High productivity in an ice melting hot spot at the eastern boundary of the Weddell Gyre

High productivity in an ice melting hot spot at the eastern boundary of the Weddell Gyre

W. Geibert,[1,2] P. Assmy,[3] D. C. E. Bakker,[4] C. Hanfland,[3] M. Hoppema,[3] L. E. Pichevin,[1] M. Schröder,[3] J. N. Schwarz,[3,5] I. Stimac,[3] R. Usbeck,[6] and A. Webb[7]

Received 27 August 2009; revised 14 January 2010; accepted 25 February 2010; published 21 July 2010.

[1] The Southern Ocean (SO) plays a key role in modulating atmospheric CO_2 via physical and biological processes. However, over much of the SO, biological activity is iron-limited. New in situ data from the Antarctic zone south of Africa in a region centered at ~20°E–25°E reveal a previously overlooked region of high primary production, comparable in size to the northwest African upwelling region. Here, sea ice together with enclosed icebergs is channeled by prevailing winds to the eastern boundary of the Weddell Gyre, where a sharp transition to warmer waters causes melting. This cumulative melting provides a steady source of iron, fuelling an intense phytoplankton bloom that is not fully captured by monthly satellite production estimates. These findings imply that future changes in sea-ice cover and dynamics could have a significant effect on carbon sequestration in the SO.

Citation: Geibert, W., et al. (2010), High productivity in an ice melting hot spot at the eastern boundary of the Weddell Gyre, *Global Biogeochem. Cycles*, *24*, GB3007, doi:10.1029/2009GB003657.

1. Introduction

[2] Oceanic processes are believed to play a pivotal role in glacial-interglacial variations in atmospheric CO_2 [*Sigman and Boyle*, 2000]. One key mechanism for changing atmospheric CO_2 is a variable exchange between the deep ocean and surface water, which is likely to be linked to ocean stratification, sea-ice cover and deep upwelling at high latitudes [*Anderson et al.*, 2009; *Francois et al.*, 1997; *Stephens and Keeling*, 2000]. Another important factor is the variation in primary production and in the silicon to carbon (Si/C) ratio of organic matter, resulting from changes in growth-limiting conditions [*Hutchins and Bruland*, 1998; *Pichevin et al.*, 2009; *Ragueneau et al.*, 2006; *Takeda*, 1998]. Iron, which is present only at trace levels in open ocean seawater has repeatedly been shown to be crucial in controlling primary production in regions where upwelling provides major nutrients in excess [*Boyd et al.*, 2007].

[3] The Weddell Gyre (WG), which constitutes the world's largest coherent deep ocean–atmosphere interface, unifies all the potential oceanic CO_2-regulating mechanisms. Furthermore, the effects of changes in nutrient uptake on atmospheric CO_2 drawdown are far more efficient in the WG than in other areas of the Southern Ocean (SO) [*Marinov et al.*, 2006]. The anticipation that sea-ice cover and ice melt patterns could change in the future increases the urgency to understand the role of the WG and seasonal ice cover in regulating atmospheric CO_2.

1.1. Eastern Weddell Gyre

[4] While clearly being a crucial factor in global climate [*Hoppema*, 2004], the WG is also a particularly intricate piece of the puzzle, because of high interannual variability in sea-ice cover and spatial structure [*de Steur et al.*, 2007; *Martinson and Iannuzzi*, 2003], and limited accessibility. One of the least investigated parts of the WG is its eastern boundary, a transition zone to the Antarctic Circumpolar Current (ACC), at approximately 20°E–35°E, south of 55°S.

[5] The few oceanographic data from the Eastern Weddell Gyre (EWG)/ACC boundary region [*Gouretski and Danilov*, 1993; *Schröder and Fahrbach*, 1999] have shown that water masses with different characteristics and momentum meet here. Remotely sensed sea surface temperature data reveal a colder northern and a warmer southern regime in the WG, together with a north–south (N–S) oriented EWG/ACC boundary in temperature at approximately 25°E (Figure 1b). This N–S oriented boundary is also seen in a southward deflection of the oceanic frontal system [*Orsi et al.*, 1995], which coincides with regional seafloor topography (Figure 1a).

[1]Grant Institute, School of Geosciences, University of Edinburgh, Edinburgh, UK.
[2]Scottish Association for Marine Science, Scottish Marine Institute, Oban, UK.
[3]Alfred Wegener Institute for Polar and Marine Research, Bremerhaven, Germany.
[4]School of Environmental Sciences, University of East Anglia, Norwich, UK.
[5]Now at the National Institute for Water and Atmosphere Research, Wellington, New Zealand.
[6]FIELAX GmbH, Bremerhaven, Germany.
[7]Department of Oceanography, University of Cape Town, Cape Town, South Africa.

0886-6236/10/2009GB003657

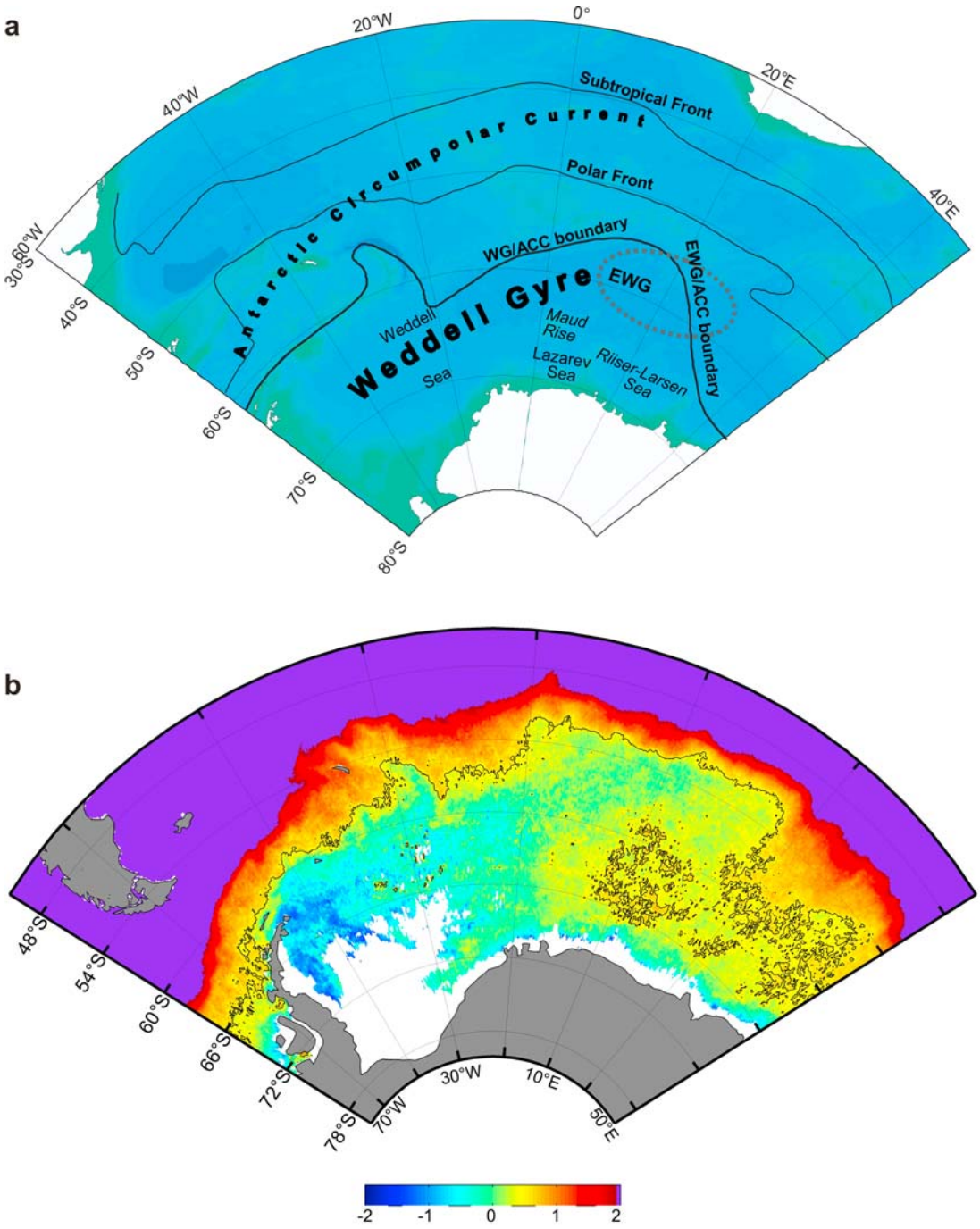

Figure 1. (a) Map of the bathymetry in the Atlantic Sector of the Southern Ocean, indicating oceanographic features (in bold font), topographic features (in italic font) and the names of regions (in normal font). Fronts and the ACC/WG boundary follow *Orsi et al.* [1995]. (b) The Weddell Gyre as seen in sea surface temperature (MODIS satellite instrument, composite of data from 2002 to 2008). The solid line indicates the 0.5°C isotherm. Note the longitudinal temperature boundary at ~25°E.

[6] According to modeling studies, the EWG region receives a certain, but not exceptionally high amount of meltwater from icebergs [*Jongma et al.*, 2009; *Schodlok et al.*, 2006], which would mainly originate in the Lazarev Sea, the Riiser-Larsen Sea, and possibly the Western part of the WG [*Gladstone et al.*, 2001]. In contrast, remote sensing data and episodic reports from shipboard observations confirm the common occurrence of icebergs in the EWG region, whereas fewer icebergs are observed further east [*Tournadre et al.*, 2008]. Icebergs have been shown to affect productivity

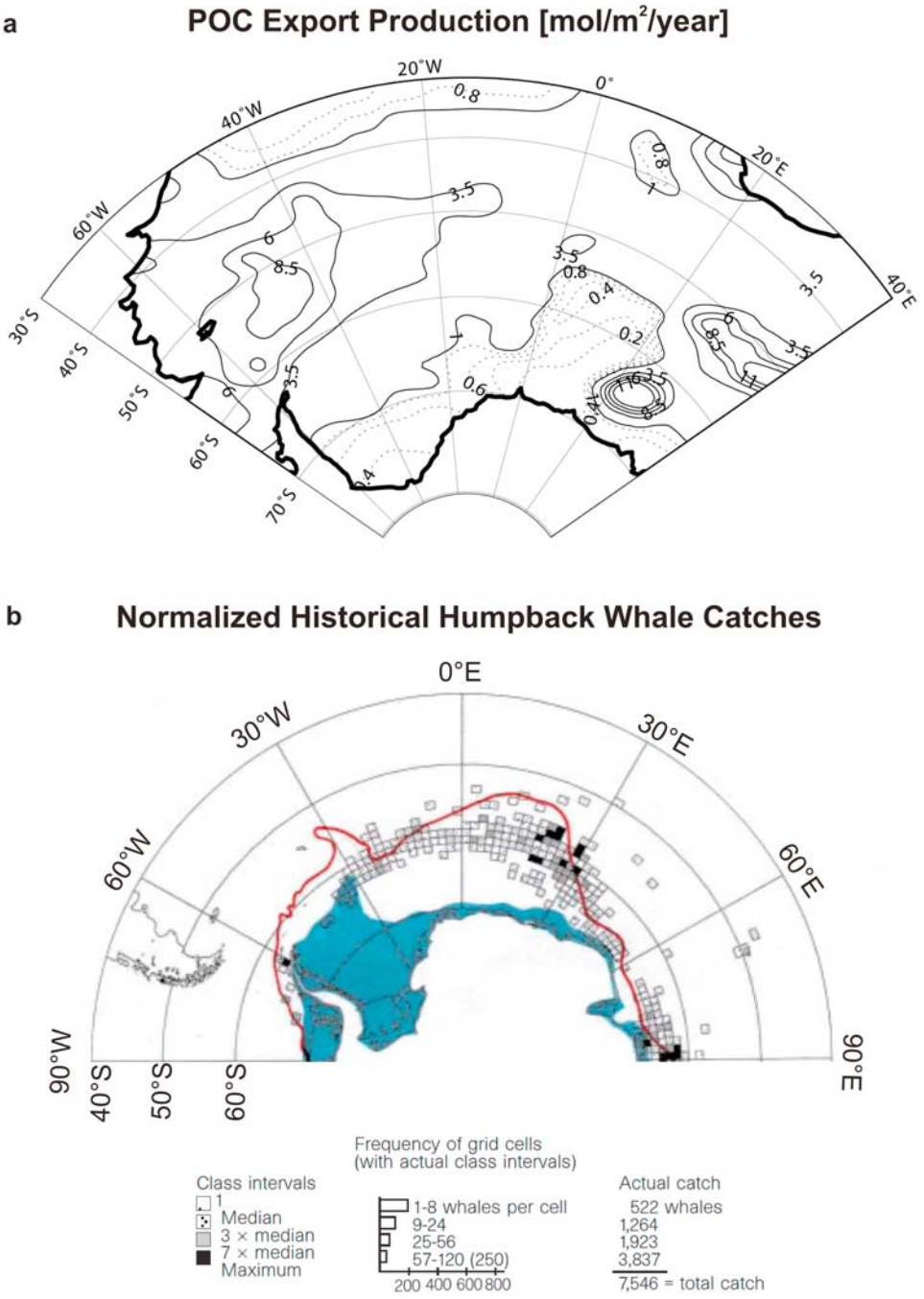

Figure 2. Indicators of bioproductivity in the WG. (a) Export production of Particulate Organic Carbon (POC) as derived by an inverse Global Circulation Model, POC export based on measured nutrient distributions, from *Usbeck et al.* [2002]. (b) Abundance of humpback whales, based on historical whale catch data [*Tynan*, 1998]; reprinted by permission from Macmillan Publishers Ltd, copyright 1998. Blue whale catches (not shown here) display a similar pattern, but the maximum abundance is found further south. Both indicators point to substantial bioproductivity at the eastern rim of the WG, at approximately 23°E, 55°S–65°S.

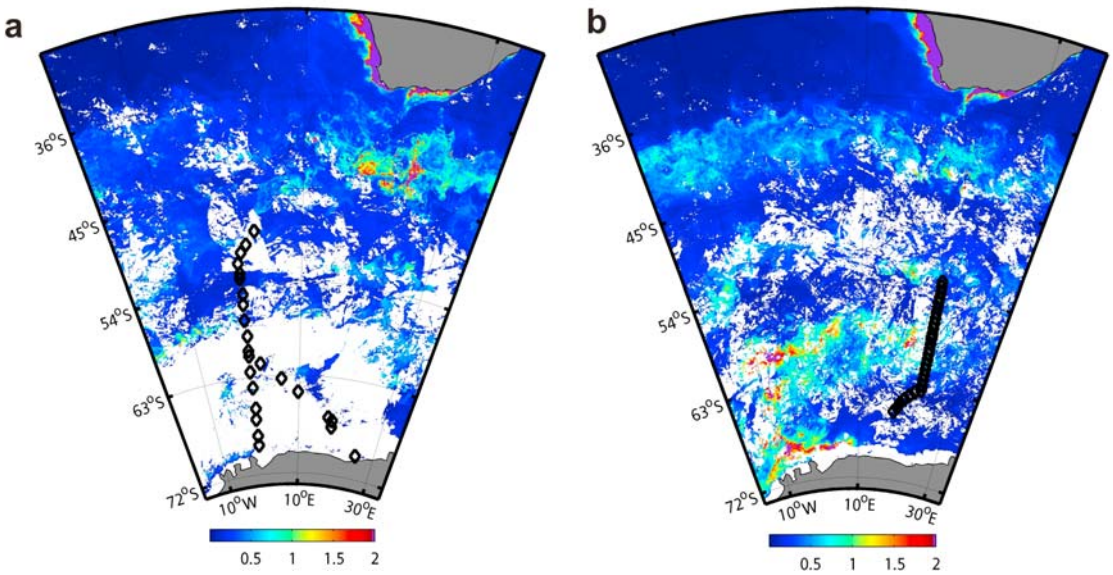

Figure 3. Composites of sea surface chlorophyll concentration in mg m^{-3} (NASA/SEAWiFS) during ANT XX/2 in (a) December 2002 and (b) January 2003. Ship's stations are shown as open symbols. White areas correspond to sea ice and/or clouds.

in the SO, though the actual effect depends on local conditions. Icebergs can lead to decreasing productivity by secondary effects on the pack ice [*Arrigo et al.*, 2002], or they can stimulate phytoplankton growth [*Smith et al.*, 2007; *Schwarz and Schodlok*, 2009].

1.2. Contrasting Indicators of Productivity at the EWG/ACC Boundary

[7] Long-term averages of ocean productivity from inverse modeling based on nutrient distributions, indicate that exceptionally high downward fluxes of organic carbon and large fluxes of silica are a permanent feature at this boundary [*Usbeck et al.*, 2002] (Figure 2a), in agreement with historic data from whale catches [*Tynan*, 1998] (Figure 2b). Whereas this maximum in ocean primary production was displayed in productivity maps prior to the satellite era [*Berger*, 1989], it has been less pronounced in recent studies using satellite data, probably because of the tendency to use monthly composites or long-term means [*Schlitzer*, 2002; *Smith and Comiso*, 2008], and because the likelihood of glimpsing high productivity amid patchy sea-ice cover and frequent cloud cover is low from satellite as compared to ship surveys. The WG in general has been shown to produce anomalously low particle fluxes to the deep ocean and the sediment due to enhanced dissolution, which prevents simple conclusions from the underlying sedimentary patterns from being drawn [*Geibert et al.*, 2005; *Leynaert et al.*, 1993; *Usbeck et al.*, 2002].

[8] If the occurrence of markedly elevated productivity levels in the EWG-ACC transition zone could be verified by in situ measurements, the question of what mechanisms support such a bloom in the open ocean, remote from any obvious iron source, would remain. Expedition ANT XX/2 was carried out on the icebreaker RV "Polarstern," to generate an in situ biogeochemical data set to complement indirect information from modeling and remote sensing techniques. Our study combines measurements of nutrient and dissolved inorganic carbon profiles, data on physical oceanography, the distribution of chlorophyll-a as seen in depth profiles and from remote sensing, the chemical composition of particles collected at the sea surface, the species composition of phytoplankton, and the distribution of the naturally occurring radioisotopes ^{234}Th and $^{227}Ac_{xs}$ to quantitatively capture the regional distribution of productivity, and to identify the controlling processes. We compare our results to previous findings and related studies in order to demonstrate the recurring nature of the observed phenomenon.

[9] The expedition to the WG took place from 24 November 2002 to 23 January 2003, consisting of a western transect in full or partial ice cover (Figure 3a), and an eastern transect at the EWG/ACC boundary at 17°E–23°E (Figure 3b). Here, we focus on the latter, which had some sea ice remaining at the southernmost stations, but ice-free conditions in the northern part [*Bakker et al.*, 2008].

2. Methods

2.1. Sampling and Analysis

2.1.1. Nutrients

[10] Polyethylene (PE) 50 mL bottles were used to collect subsamples from Niskin bottles for nutrient analysis. The PE bottles were rinsed three times with the sample water. The samples were poisoned with 105 μg/mL mercuric chloride ($HgCl_2$), stored at 4°C and analyzed at the home laboratory 7 months after sampling. This preservation method has been shown to be successful for the storage of nutrient samples for up to 2 years [*Kattner*, 1999]. A Technicon autoanalyser II

was used to measure the concentrations of Si, NO_x^-, NO_2^- and NH_4^+ using standard techniques [*Grasshoff and Ehrhardt*, 1983]. All the samples were analyzed in duplicate and the average difference of the duplicates from the mean was 0.23% for NO_3^- and 0.26% for Si.

2.1.2. Oxygen

[11] Samples for oxygen analysis were the first to be drawn from the Niskin bottle unless chlorofluorocarbon (CFC) samples were taken. Volume calibrated glass bottles of ~120 mL were used. A piece of Tygon tube was attached to the outlet tap of the Niskin bottle to allow the water to enter the sample bottle with minimum air contact and turbulence. The sample was allowed to overflow up to three times the bottle volume and the temperature of the seawater was then measured. The oxygen was chemically fixed and the bottles were capped and shaken. Samples were analyzed using the standard Winkler method [*Grasshoff and Ehrhardt*, 1983] within 12 h of collection. Whole bottle titrations were performed as recommended for WOCE [*Culberson*, 1994]. The titration process was automated and the endpoint calculated using an electronic burette and photometer linked to a computer (SiS GmbH Dissolved Oxygen Analyzer). Duplicate samples were drawn and analyzed for 10% of all the samples. The analytical precision of these duplicates was 0.45%.

2.1.3. Pigments

[12] Phytoplankton samples were taken by filtering seawater samples from Niskin bottles onto precombusted GF/F filters. All samples were taken in duplicate or triplicate. Filters were stored in liquid nitrogen until analyzed in the home laboratory. Phytoplankton pigment concentration was measured by high-performance liquid chromatography (HPLC) [*Wright et al.*, 1991]. The HPLC system comprised a Waters 600E Controller, Waters 717 plus Autosampler, Techlab column oven (maintaining a temperature of 30°C), Waters Spherisorb ODS-2 column (250 × 4.6 mm, 5 μm packing) and Waters 996 Photo Diode Array detector. All solvents were HPLC-grade (Chromoscan Inc.). Pigments were extracted by placing the filter together with 20 μL internal standard solution (canthaxanthin, Roche pharmaceuticals, in 100% DMF), 0.5 mm zirkonia beads (Biospec Products Inc.) and 600 μL > 99% acetone into a conical-tipped vial and shaking for 50 s at 50,000 rpm in a MiniBead BeaterTM (Biospec Products Inc.). Extracted pigments were separated from filter debris by centrifugation at 3500 rpm for 3 min, followed by 1 min at 10,000 rpm, with the centrifuge cooled to 0°C. 180 μL of the eluent were added to a 250 μL glass insert within a sprung brown-glass HPLC vial together with 45 μL 1M ammonium acetate buffer, and 180 μL of this final solution was injected into the HPLC. The HPLC chlorophyll-a peaks were calibrated against pigment standards from the International Agency for ^{14}C Determination, Denmark.

[13] Optical measurements of chlorophyll-a (chl-a) were obtained in situ with a Seapoint Fluorometer at a vertical resolution of <1 m. The optical measurements (F, in arbitrary units) from the nearest 1 m depth bin of the CTD upcast were calibrated against the discrete HPLC measurements, giving the linear equation

$$\text{chl-a} = 168.4[\pm 6.54] \times \text{F} \quad (1)$$

The linear correlation of HPLC and in situ fluorometer data was found to explain 76% of the variance (n = 61). Some evidence of time dependence was found, with fluorescence efficiency apparently depressed during high solar zenith, but the difference was insufficient to justify the application of a time-dependent calibration. The reported values are optical measurements by fluorometry, from 1 m depth-binned downcasts, as calibrated using equation (1).

2.1.4. Large-Volume Phytoplankton Samples as Obtained by a Continuous Flow Centrifuge (Composition of Suspended Matter, Species Overview)

[14] At selected stations, large-volume samples of particulate matter were taken from the ship's seawater supply with a continuous flow centrifuge (Padberg Z61), fitted with a trace element clean introduction and separation system [*Schussler and Kremling*, 1993]. With this system, particles are deposited at 17,670 × g onto an acid-cleaned Teflon® sheet. Sample volumes (868–3507 L) were recorded with a flowmeter. The samples were freeze-dried, then analyzed for C, N and S contents. Biogenic silica content was determined by continuous leaching [*Mueller and Schneider*, 1993]. Total iron concentrations were determined by Inductively Coupled Plasma Optical Emission Spectroscopy (ICP-OES). The procedural blank contributed 0.6–2.5% to the values. Reproducibility was monitored by reference material HISS-1 (marine sediment from Hibernia Shelf, National Research Council Canada). Control samples were run after partial and complete cleaning of the diatom frustules from organics and clay to exclude external contamination. A potential contamination on some of these samples was as also excluded via inspection by SEM. Aliquots of the phytoplankton samples were investigated for species composition in order to identify potentially bloom-forming diatoms (details below).

2.1.5. Physical Oceanography

[15] Temperature and salinity were recorded with a Seabird SEACAT SBE 19 instrument. Here, we report 5 m averages. Bottle data were related to the salinity and temperature of the nearest 5 m data point. A comparison of the physical data with that from another CTD instrument, which was operated in parallel and continuously calibrated against seawater standards (M. Schröder et al., The structure of the eastern Weddell Sea warm inflow, manuscript in preparation, 2010) yielded excellent agreement.

2.1.6. Radionuclides

[16] The $^{234}Th/^{238}U$ disequilibrium in productive surface waters has proven to be a useful indicator of particle export from the euphotic zone [*Cochran and Masqué*, 2003; *Savoye et al.*, 2006]. We measured the disequilibrium according to an established method [*Rutgers van der Loeff and Moore*, 1999]. Briefly, water samples of 20 L were filtered (142 mm diameter, 1 μm pore size Nucleopore) immediately after recovery. The filters were dried and folded, and particulate ^{234}Th was counted directly on the filters via beta counting while on board. Appropriate corrections for self absorption were applied. In the dissolved fraction, a precipitate of MnO_2 was generated, which was quantitatively recovered on filters (analog to the particulate fraction). The counting procedure was identical to that used for the particulate fractions. Again, suitable self-absorption corrections were applied. No external yield tracer was used. A set of deep samples (400 m) in full

radioactive equilibrium was taken to calibrate the method. Quantitative recovery was controlled by monitoring ^{234}Th equilibrium in the deepest sample. After the cruise, all samples were recounted after decay of ^{234}Th for the determination of background contributions from other nuclides. ^{238}U was calculated from salinity [*Rutgers van der Loeff and Moore*, 1999]. The integrated deficit of ^{234}Th was taken as a measure of particle export. Based on a given $C_{org}/^{234}$Th ratio, ^{234}Th depletion could be converted into an estimate of C_{org} export. A substantial component in the calculation of ^{234}Th-based carbon export is the choice of an appropriate model for representing steady state or nonsteady state conditions [*Savoye et al.*, 2006]. In our case, we selected a special version of nonsteady state conditions, assuming that particle export during the winter season under the ice was negligible; therefore ^{234}Th would be in equilibrium with ^{238}U. The assumption that ^{234}Th is close to secular equilibrium during the winter months is supported by our findings from the ice-covered transect at 0°E during the same expedition. Sea-ice retreat occurred during December, which allows some export to have happened several weeks before sampling, while our model implicitly assumes that export production prior to sampling was insignificant. In the event that export production was actually high before the austral spring, the ^{234}Th export estimates will therefore be subject to a negative bias; that is, this method underestimates production. The resulting model simply translates the integrated deficit of ^{234}Th (measured in disintegrations per minute, dpm) into an export of C by means of the $C_{org}/^{234}$Th ratio. The $C_{org}/^{234}$Th ratio in particles was obtained by direct measurements of particulate ^{234}Th ($^{234}Th_{part}$), combined with C contents for the individual samples that were derived from fluorometrically determined chlorophyll-a (chl-a). The relation C_{org}/chl-a was determined by means of discrete C_{org} samples from the large volume centrifuge (as described above). Based on this relation, particulate C_{org} was calculated for each ^{234}Th value. The resulting $C_{org}/^{234}$Th values on particles were found to be highly variable, from 1.2 to 80.0 μmol C_{org}/dpm ^{234}Th, with an average of 11.7 μmol C_{org}/dpm ^{234}Th. By multiplying the ^{234}Th deficit of a depth interval with the respective $C_{org}/^{234}$Th ratio on particles, a C_{org} export could be derived. Adding up all positive C_{org} exports at the surface, we can derive an integrated C_{org} export at the ^{234}Th stations. Negative export values may occur due to remineralization of ^{234}Th at greater depths, which leads to excess ^{234}Th [*Usbeck et al.*, 2002].

[17] $^{227}Ac_{xs}$ is a tracer that can be used to reveal inputs of deep water to the surface in open ocean waters. This isotope, with a half-life of 21.77 years, has a very dominant source at the deep-sea floor [*Geibert et al.*, 2008]. Its half-life does not usually allow it to reach the upper water column [*Nozaki*, 1984, 1993], and the Weddell Gyre is a remarkable exception to this rule, illustrating the rapid upwelling of deep waters. Only surface waters that have very recently been formed through upwelling from greater depths can display high $^{227}Ac_{xs}$ values. Surface waters in the WG have been found to contain a unique signature of $^{227}Ac_{xs}$ of ~0.5 dpm/m^3, whereas values for ACC surface waters are near 0.25 dpm/m^3 [*Geibert et al.*, 2002]. The ^{227}Ac was collected in samples from the ship's seawater supply. Two sequential polypropylene filter cartridges coated with manganese dioxide were used to extract ^{227}Ac from the seawater. The filter cartridges were acid-leached with 6 N hydrochloric acid in a Soxhlet extraction system, in the presence of a ^{229}Th/^{225}Ac spike. The chemical separation and detection of ^{227}Ac followed previously published procedures [*Geibert and Vöge*, 2008; *Geibert et al.*, 2002].

2.1.7. CO_2

[18] The description of CO_2 dynamics from the expedition has already been published [*Bakker et al.*, 2008]. In the present study, we use the TCO_2 data to constrain C drawdown independently from the nutrient budget. Briefly, TCO_2 is the sum of all inorganic carbon species dissolved in the ocean, also known as DIC. It is measured using the precise coulometric technique. All samples were measured in duplicate or triplicate. The precision was estimated to be ±1.8 μmol kg^{-1}, while the accuracy, set by internationally recognized Certified Reference Material (CRM), was ±2.5 μmol kg^{-1}.

2.1.8. Species Composition

[19] The species composition is based on the relative contribution of each species/genus with respect to the total community and relies on semiquantitative abundance estimates. This information on species composition was obtained from the large-volume centrifuge samples (see method description above), which does not preserve species without a hard shell. The microscopic examination of the large-volume centrifuge samples is therefore biased toward diatoms that are encased by resistant silica cell walls. However, since diatoms are the almost exclusive bloom formers and the major exporters of organic matter to subsurface waters in the Southern Ocean, they are a good indicator of the productivity regime prevalent at the respective sites of this survey.

[20] An aliquot of the plankton samples was preserved with hexamine-buffered formaldehyde at a final concentration of 2%. Samples were settled in 3 mL sedimentation chambers (Hydrobios, Kiel, Germany) for at least 2 h. Cells were identified and enumerated using inverted light and epifluorescence microscopy (Axiovert 200, Zeiss, Oberkochen, Germany) according to the method of *Utermöhl* [1958]. Organisms were counted at magnifications of 200–400× according to the size of the organisms examined.

2.2. Data Processing and Calculations

2.2.1. Calculating the Amount of Sea-Ice Meltwater

[21] At the time of sampling, the sea-ice cover was already absent at the EWG/ACC boundary [*Bakker et al.*, 2008] for all but the southernmost stations. A corresponding meltwater signal could be identified as decreased salinity, combined with elevated sea surface temperatures (Figure 4). In order to assess the input of melting ice quantitatively, we use the salinity minimum at the surface compared to the underlying Winter Water (WW, salinity here 34.05). In Table 1, we report the thickness of melting sea ice required to explain the integrated salinity deficit at the sea surface (same transect as Figure 4, see track in Figure 3b). The calculation is based on a sea-ice salinity of 5, as estimated from earlier sea-ice salinity profiles from the WG [*Eicken*, 1992]. The average density of sea ice with snow cover was

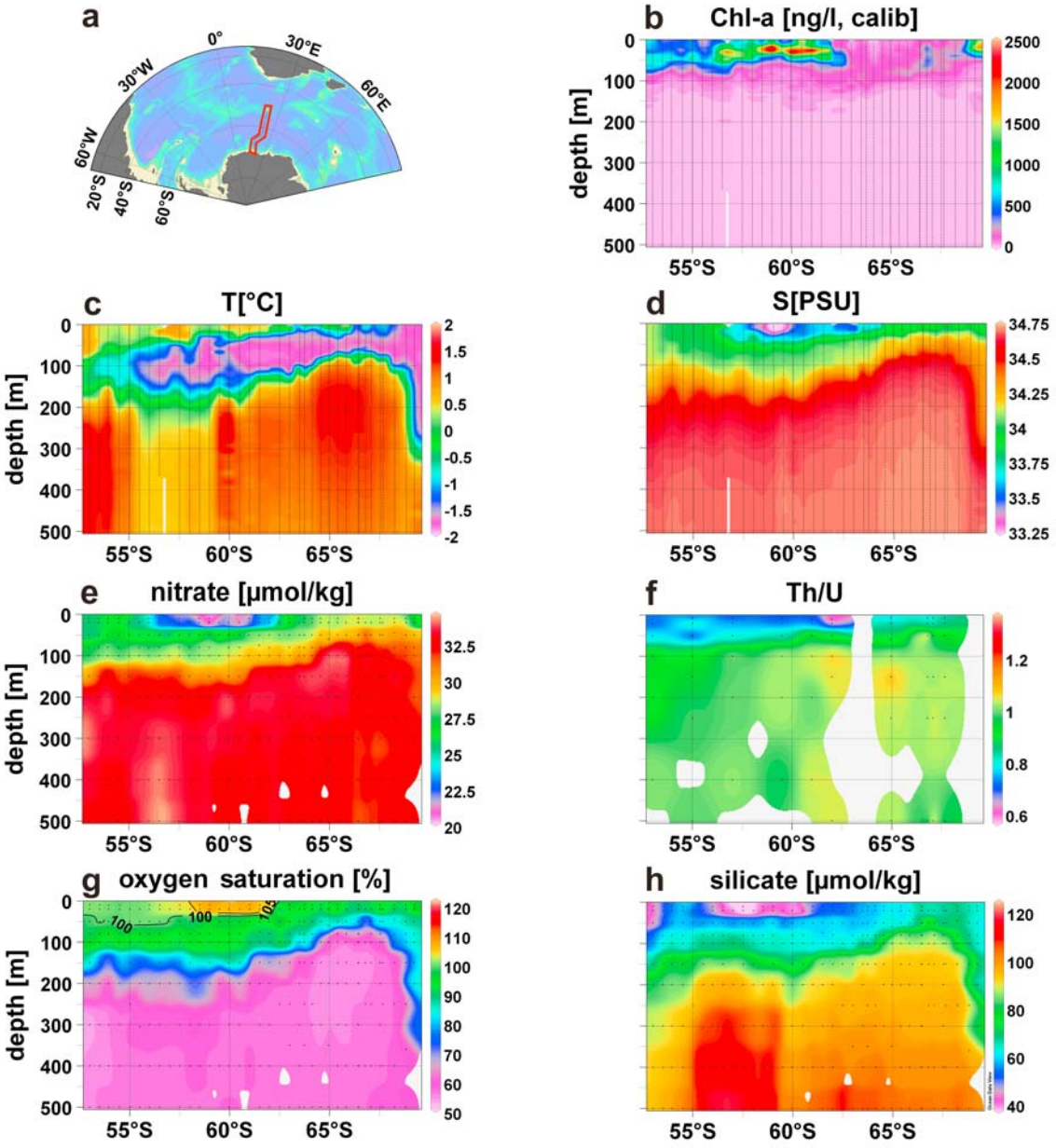

Figure 4. (a) Results for a section along the EWG boundary (together with bathymetry) in December 2002/January 2003. (b) A substantial concentration of chl-a is found between 62.5°S and 57.5°N. This signal is associated with a (c) surface temperature maximum and (d) salinity minimum, which indicate the role of melting ice. (e) Nitrate (μmol/kg) and (h) silicate (μmol/kg) are depleted due to phytoplankton growth, and (f) $^{234}Th/^{238}U$ ratios <1 indicate that particles have been exported from the surface layer. (g) Oxygen saturation values >100% are evidence of photosynthetic activity. Figure generated with Ocean Data View software (R. Schlitzer, Ocean Data View, 2007, available at http://odv.awi.de).

assumed to be 815 g/L, based on a keel-to-sail ratio of 4.4, as reported by [*Worby et al.*, 2008].

2.2.2. Assessing Productivity

[22] The synoptical approach of our study allows us to constrain production in various ways. Here, we explain the approaches, compare the respective results, and summarize the implications for bioproductivity. Briefly, the assessment of productivity is based on (1) the integrated depletion of nutrients; (2) the balance of the carbonic acid system; (3) pigment distribution, both from stocks found in situ, a chl-a based in situ primary production algorithm, and from a satellite perspective; and (4) with a comparatively coarse

Table 1. Estimates of Production, Freshwater Input Due to Melting Ice, and Concentration (Activity) Data for the Isotope $^{227}Ac_{xs}$ at the Sea Surface[a]

Station (PS63/)	Date (2003)	Lon °E	Lat °N	Sea-Ice Thickness Equivalent (mm)	Si Production From Si Deficit (mmol/m^2)	PP From NO_x Deficit (mmol/m^2)	PP From TCO_2 Deficit (mmol/m^2)	PP From in Situ Chl-a, Depth-Integrated (mmol/m^2)	PP From in Situ Chl-a 10 m VGPM (28 Days) (mmol/m^2)	PP From MODIS VGPM (Last 28 Days) (mmol/m^2)	EP From ^{234}Th (mmol/m^2)	Fe/C (mol/mol)	$^{227}Ac_{xs} \pm 1\ \sigma$ (Surface) (dpm/m^3)
119-01	6 Jan	17.76	−65.83	143	14	24		140	108	249			
120-02	7 Jan	18.49	−65.41	257	50	52		157	148	248			
121-02	7 Jan	19.02	−64.96	192	20	19		149	164	222	145	0.0002	0.38 ± 0.06
122-01	8 Jan	19.81	−64.56	171	4	2		149	230	220			
123-02	8 Jan	20.76	−64.13	585	184	214	26	114	59	211			
124-01	8 Jan	21.74	−63.75	413	264	364	32	203	96	251			
125-01	9 Jan	22.99	−63.50	340	201	275	103	169	149	276			
126-01	9 Jan	22.99	−63.00	591	405	609		164	76	406			
127-01	9 Jan	23.00	−62.50	622	349	859	344	350	108	700		0.0004	0.25 ± 0.05
128-01	9 Jan	22.99	−62.00	512	322	1254	1097				2018		
130-01	10 Jan	23.00	−61.50	563	446	1301	1187	724	690	903			
131-01	10 Jan	23.00	−61.00	665	446	1720	1740	939	326	1009	504		
133-01	10 Jan	23.02	−60.50	986	844	2113	1978	881	1119	926			
134-01	11 Jan	22.99	−59.96	1061	887	2020		806	547	614			
135-01	11 Jan	23.01	−59.50	1255	1022	2242	1344	546	1203	746	594		
137-01	12 Jan	23.01	−59.00	1341	639	2150	1928	599	1028	666			
138-01	12 Jan	23.00	−58.50	1292	804	2115	1593	618	666	614			
139-01	12 Jan	23.00	−58.31									0.0002	0.22 ± 0.06
140-01	12 Jan	22.99	−58.02	811	1090	2349	1065	589	844	529			
141-01	13 Jan	23.00	−57.51	895	1051	2022	1143	772	1024	674			
142-01	13 Jan	22.99	−57.01		932	2033	1567	706	153	771	905		
143-01	13 Jan	23.01	−56.50	515	919	2264	1519	988	701	741		0.0002	0.60 ± 0.07
144-01	14 Jan	23.00	−56.00	239	457	1640	954	473	579	747			
145-01	14 Jan	23.02	−55.51	234	600	1555	914	379	211	684			
146-01	14 Jan	23.00	−55.32									0.0002	0.98 ± 0.09
147-01	14 Jan	23.01	−55.01	105	281	1453	906	425	645	600	1116		
148-01	14 Jan	23.00	−54.50	228	136	1249	672	418	449	516			
149-01	15 Jan	23.05	−53.95	103	238	955	323	337	471	482			
150-01	15 Jan	23.01	−53.49	69	678	1693	1052	490	209	544			0.26 ± 0.05
152-01	15 Jan	22.99	−53.00		1877	1900	1248	624	570	592	1158	0.0002	0.58 ± 0.07

[a]Methods and the associated uncertainties are discussed in the text. Primary production (PP) is given in units of C, and Si production is given in units of Si.

resolution, we can assess export production by combining ^{234}Th data and the data from large-volume centrifuge samples. The results are presented in Table 1; we discuss the different approaches below.

[23] 1. In a similar approach to *Hoppema et al.* [2002], we first determine the nutrient concentration prior to the onset of the bloom. We assume that the Winter Water (WW) at 23°E (T < −1.76°C) represents the initial conditions; the WW is found here as a temperature minimum below the warmer surface layer (Figure 4). We obtain 28.7 ± 0.4 μmol/kg for NO_3^- (n = 10) and 61.7 ± 1.8 μmol/kg for Si (n = 10) as the starting point. We attribute deficits in nutrient concentrations compared to the concentration in WW to primary production. Based on the vertical distribution of nutrient concentrations, we can calculate an integrated deficiency for NO_3^- and Si, respectively, in mmol/m^2. Assuming a constant Redfield value (106:16) for the molar C:N uptake ratio in the Weddell Sea [*Hoppema and Goeyens*, 1999], as supported by the findings from large volume particulate samples from this cruise, we calculate the organic carbon (C_{org}) production at 23°E. C_{org} production in the bloom is consistently found to be about 2000 mmol m^{-2}, silicon production is about 1000 mmol*m^{-2}. The values integrate production for the whole productive season up to the sampling date. They reflect the net community production (NCP), which is lower than the net primary production.

[24] 2. We can calculate the difference between the sum of all dissolved inorganic carbon species (TCO_2) in WW (2183.52 ± 8.11 μmol kg^{-1}, n = 8, for T ≤ −1.76°C and latitude > −65°S) and measured TCO_2 profiles above WW. The depth-integrated difference of TCO_2 compared to WW after normalization to a salinity of 35 can then be interpreted as carbon consumption by primary production, again reflecting NCP. These values are given for comparison with the production as derived from nutrients, but the uncertainty associated with the underlying assumptions should be taken into account. In particular, this approach does not consider exchange with the atmosphere, so values will become less reliable with increasing elapsed time since the onset of spring production. Uptake of CO_2 from the atmosphere will generally tend to cause a slight underestimate of production. We also implicitly neglect the potential effect of calcification. We assume the presence of a WW layer that is homogenous in TCO_2, irrespective of the latitude, while in fact some of the reported standard deviation of the WW signal may be due to a latitudinal trend. Moreover, the normalization procedure, necessary to correct for dilution by sea-ice melting, neglects the TCO_2 content of sea ice, possibly also leading to an underestimate of production. While these error sources might cause a possible bias of the primary production estimate, most likely toward an underestimate, the potential bias is smaller than the large signal we observe.

[25] 3a. Measured in situ chlorophyll-a (chl-a) fluorescence was calibrated against chl-a as measured by HPLC on discrete samples (see section 2). No filtered samples were taken for C_{org} analysis. Instead we used large-volume centrifuge samples for C_{org} and individual chl-a values from the nearest in situ fluorometer measurement to calculate an empirical C_{org}–chl-a relationship. The values presented in Table 1 were obtained by vertically integrating the stock of chl-a, and multiplying this value with the empirical factor

$$C_{part}[\mu mol/L] = 0.0104 * chl\text{-}a[ng/L] \quad (r^2 = 0.84, n = 10)$$

This corresponds to a C/chl-a ratio of 125 mg/mg, which is well within the range of previously reported data from the Southern Ocean [*Garibotti et al.* 2003]. If grazing and mortality/export were negligible, and chl-a was close to zero during winter, then the depth-integrated chl-a stock would represent the cumulative production for the sampling season. If phytoplankton cells were released to the water from melting sea ice and were retained in the surface waters, then this method yields an overestimate of seasonal production. If export has taken place, as we explore below, this value underestimates true production.

[26] 3b. Daily primary production was calculated for each station using the vertically generalized production model [*Behrenfeld and Falkowski*, 1997]. Surface chl-a was taken from the calibrated fluorometry profiles at 10 m, daily insolation from the standard 9 km SeaWiFS product, P^B_{opt}, the maximum carbon fixation rate within the water column, was calculated using CTD-measured surface temperatures [*Behrenfeld and Falkowski*, 1997], euphotic zone depth was calculated using each chl-a profile [*Morel and Berthon*, 1989] and the number of daylight hours was calculated [*Kirk*, 1994]. Daily production was multiplied by 28 days to give an estimate of seasonal production comparable to the nutrient results.

[27] 3c. Eight day production estimates provided by the NASA-affiliated Ocean Productivity Team were taken for the 4 closest weeks during which each pixel was cloud- and ice-free. For each station, these four daily productivity values were multiplied by 7 days and summed to give a 28 day production estimate for comparison with the other methods.

[28] 4. Because of the 24 day half-life of ^{234}Th, the ^{234}Th-derived export production reflects only the particles that have recently been removed from the surface. Therefore, they should be similar or lower than the estimates obtained by other approaches. With the exception of station PS63/128–1, which is anomalously high, the ^{234}Th-based export production is lower than the nutrient-derived primary production, while confirming the exceptional productivity levels in the bloom.

2.2.3. Exploring the Differences Between the Productivity Estimates

[29] The estimates from nutrient depletion are considered to be very reliable, as long as the surface waters are fed by WG Winter Water (WW) or the local ACC waters, which have very similar nitrate contents. This assumption holds for the entire bloom area, which yields consistent production values from all calculation approaches. It is less valid for the southernmost stations, which are located in the vicinity of the Antarctic Coastal current that brings waters from the east.

[30] The production data from TCO_2 should not be taken as absolute values, as uptake from the atmosphere may have altered them, causing an underestimate [*Bakker et al.*, 2008]. They also respond strongly to the assumptions of a WW

origin, as nearby ACC water has a different TCO_2 content to WW. Where the prerequisites are met, the production data from TCO_2 clearly confirm the findings from the nitrate distribution.

[31] The production estimates from in situ chlorophyll-a (chl-a) (Figure 4) depend on the accuracy of the fluorometer calibration, and on the organic carbon (C_{org}) versus chl-a conversion factor, which has been determined using a limited number of stations. This adds some uncertainty to the absolute production results, while being a reliable indicator for qualitative changes. The in situ estimates of the Vertically Generalized Production Model (VGPM) are significantly, but not tightly correlated with in situ, depth-integrated chl-a stocks ($r^2 = 0.426$, n = 27). The major uncertainty for this method is the length of the productive season, combined with temporal variability in surface chl-a. If the calculations are repeated for an assumed productive season lasting 90 days, then the VGPM estimates agree well with the nutrient-based estimates, whereas for a 28 day productive season, the VGPM values are much lower than the nutrient-based estimates (VGPM = nutrient • 0.2243[±0.03] + 245[±42], $r^2 = 0.637$, n = 28), suggesting that the satellite did not capture the highest chl-a values. Both in situ and satellite-based VGPM results are affected by uncertainty in the maximum rate of photosynthesis (P^B_{opt}), which ranged from 1.1 to 6.6 mg C (mg chl-a)$^{-1}$ h^{-1}, when calculated using the CTD data [*Behrenfeld and Falkowski*, 1997]. This is within the range reported previously for low-temperature waters [*Behrenfeld and Falkowski*, 1997]. Another critical factor affecting satellite-derived estimates is the correlation between surface chl-a and depth-integrated chl-a, which was good for this data set ($r^2 = 0.624$, n = 34); that is, there was no "invisible" deep chlorophyll maximum at the time of sampling. ^{234}Th-export data agree well with the other production data, as they are expected to be a certain fraction of the primary production. In summary, all production estimates yield comparable results for the bloom area, where the model assumptions are met best.

3. Results: Sea Ice and Primary Production

[32] The results as reported in Table 1 indicate a maximum of meltwater at three stations just north of 60°S, corresponding to an average sea-ice thickness of ~130 cm. We compare this observed value to the previously reported local sea-ice thickness. For the EWG in winter, on a >10 year average, typically 89% of the sea surface is covered by 54 ± 37 cm sea ice, corresponding to 48 cm for 100% cover [*Worby et al.*, 2008]. The observed meltwater of up to 130 cm therefore represents 2.7 times the typical sea-ice thickness for this region. We must consider the possibility that the freshwater lens has spread horizontally, in which case the factor 2.7 is an underestimate of the actual meltwater contribution. At most stations in the region influenced by meltwater, no notable mixed layer was present, as large gradients in temperature and salinity were observed even in the uppermost layers (Figures 4c and 4d). Most chlorophyll maxima in the bloom region were seen between 20 and 40 m depth (Figure 4b).

[33] Primary production was estimated using a variety of approaches based on independent data sets, detailed in section 2. An intense bloom with substantial productivity is detected by all approaches (Table 1). The nutrient distribution (Figure 4) locates the most intense bloom between 62.5°S and 56.0°S, coinciding with the region of maximum meltwater input. The production of organic carbon (C_{org}) in the bloom as indicated by nitrate deficits is consistently found to be about 2000 mmol*m^{-2}, (Table 1). Silica production is about 1000 mmol*m^{-2}. These values integrate production for the whole productive season up to the sampling date, and they reflect the net community production (NCP), which is lower than the net primary production.

[34] The well constrained N–S extent of the bloom is approximately 600 km; the E–W extent was estimated to be at least 1000 km in January, based on the surface distribution of chl-a (Figure 3), which means the bloom covers an area of >600,000 km^2, about as large as the northwest African upwelling region at maximum extent [*Helmke et al.*, 2005].

[35] The productivity levels (2000 mmol/m^2 in a period of ~1 month) are comparable to those of blooms found in naturally iron-fertilized coastal or island Antarctic environments, and they are higher than in artificially iron-fertilized patches [*Bakker et al.*, 2007]. The observed bloom also resembled natural [*Kang and Fryxell*, 1993; *Smetacek et al.*, 2002] and artificially iron-induced blooms [*Assmy et al.*, 2008; *Assmy et al.*, 2007; *Tsuda et al.*, 2003] in the prevalence of *Chaetoceros* species within the bloom area.

[36] The complete in situ data and results on species composition can be obtained from the Pangaea database (http://doi.pangaea.de/10.1594/PANGAEA.726958).

4. Discussion

4.1. High Productivity and Low Salinity in the EWG

[37] Our results present strong evidence for the existence of substantial bioproductivity at the EWG/ACC boundary. The previous identification of such a region by inverse modeling [*Usbeck et al.*, 2002], high biogenic silica fluxes to the underlying sediment [*Geibert et al.*, 2005], and high whale abundances [*Tynan*, 1998] strongly suggests that this is a recurrent feature, though variable in location and extent, because the location of the boundary wanders longitudinally between years (indicated by patchiness around the 0.5°C isotherm in Figure 1).

[38] The salinity minimum in the EWG, which is too pronounced to be fed from any local water mass, has not only been observed in this season, but it has also been found in other studies, e.g., expedition Polarstern ANT XVI/3 [*Boye et al.*, 2001], or the recent ANDREX study (D. C. E. Bakker, personal communication, 2010). We therefore conclude that excess melting ice is also a recurrent phenomenon in the EWG.

[39] Our results show that the productivity is linked to melting ice at the sea surface. The link between melting sea ice and phytoplankton blooms has been described previously [*Savidge et al.*, 1996; *Smith and Nelson*, 1985; *Sokolov*, 2008]. However, it has been demonstrated that stratification due to sea ice alone is not sufficient to generate large phytoplankton blooms [*Bathmann et al.*, 1997]. Consequently, we must not only consider the role of melting sea ice for increased

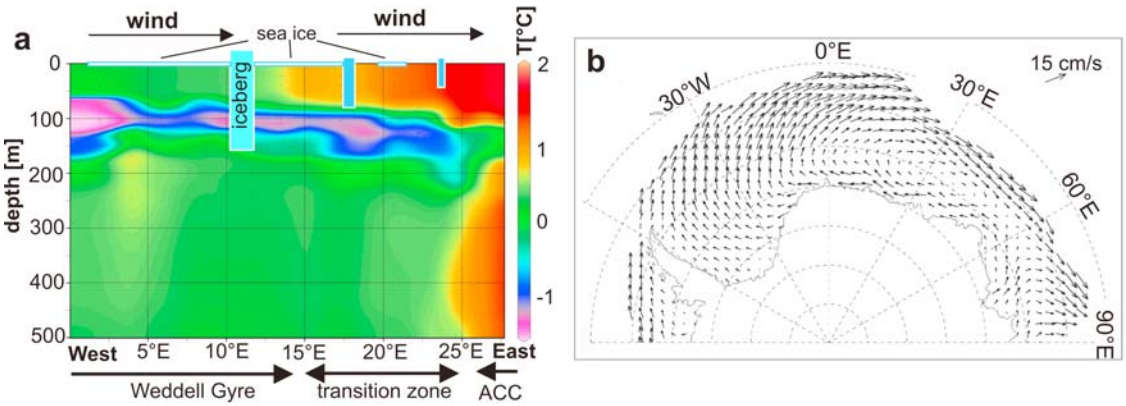

Figure 5. (a) Schematic drawing of the proposed mechanism for enhanced sea ice and iceberg melting at the EWG/ACC boundary. Note that the underlying graph of temperature distribution is not based on data from this expedition, which were mainly oriented in the S–N direction, but were taken from World Ocean Circulation Experiment line SO4 (source: electronic atlas of World Ocean Circulation Experiment data, available at http://www.ewoce.org). This transect is mostly W–E directed, following the prevailing wind direction in the Southern Ocean. The latitude ranges from ~58°S (W) to 54°S (E). Our in situ transect (Figures 3b and 4) is oriented perpendicularly to this section, intersecting at 23°E. (b) Mean ice motion for 10 years in a polar stereographic projection. Sea ice and enclosed icebergs will be forced eastward by wind pressure, where they reach the warmer waters of the ACC, which float on top of WG WW. This causes enhanced melting of ice at the EWG/ACC boundary. Modified after *Kimura* [2004], with permission.

stratification of surface waters, but also for the enhanced supply of limiting micronutrients, especially iron. We will therefore focus our discussion on two specific aspects of the observations. First, we explore mechanisms that might explain why the EWG/ACC boundary receives consistently more freshwater (from sea ice or icebergs) than other regions of the SO, and second, we investigate how this may relieve iron limitation.

4.2. Enhanced Supply of Ice to the EWG Boundary

[40] Freshwater supply to the EWG/ACC boundary is controlled by sea ice, icebergs and precipitation (mainly onto sea ice). Sea-ice transport in the WG generally follows wind-forcing, which results in a general pattern of eastward transport in the northern WG [*Kimura*, 2004; *Uotila et al.*, 2000], see Figure 5b. For most parts of the WG, the atmospheric circulation patterns roughly coincide with the ocean circulation, which means that sea ice remains within the same water mass. The EWG/ACC boundary is an exception to this rule. Here, a longitudinal boundary in surface water masses is found at ~25°E (Figure 1), across which sea ice drifts under wind-forcing (see Figure 5). This situation holds not only in spring, but also persists in winter, then slightly further northeastward, leading to enhanced sea-ice melting rates at the EWG/ACC boundary. With ice drift velocities of 15 cm/s [*Kimura*, 2004] and an average ice thickness of 48 cm [*Worby et al.*, 2008], approximately 42 L of sea-ice volume cross each meter of this boundary per minute.

[41] Icebergs might be expected to follow the circulation of the underlying water masses, as they penetrate to considerable water depths, whereas the cross-sectional area exposed to wind is comparatively small. However, a combination of observational data and modeling has shown that even large Antarctic icebergs follow the wind-drifted sea ice in which they are enclosed [*Lichey and Hellmer*, 2001]. Therefore, a closed sea-ice surface in the winter months also means wind-driven icebergs, which are exposed to higher water temperatures at the EWG/ACC boundary, representing a permanent melting hot spot for wind-drifted ice, as depicted in Figure 5.

[42] This advective mechanism explains why the eastern rim of the Weddell Gyre consistently receives an excess of freshwater from melting ice, potentially both icebergs and sea ice.

[43] In order to disentangle the proportions of sea ice versus icebergs, we compare our salinity data to a recent modeling study [*Jongma et al.*, 2009]. Jongma et al. have investigated the potential salinity decrease resulting from melting icebergs in the Southern Ocean. In the region that is affected most by melting icebergs according to their study, Jongma *et al.* report a salinity decrease of up to 0.3 units, with typical values in the WG of around 0.1. In contrast, we observe a salinity decrease of up to 1.5 units compared to local water masses. We conclude that, from a modeling perspective, icebergs alone would not be sufficient to produce the salinity minimum found in the EWG, and sea ice must be the main actor. There is, however, episodic shipboard evidence of high iceberg densities in the region, which partly agrees with satellite observations that suggest a decrease in iceberg density east of the EWG/ACC boundary [*Tournadre et al.*, 2008], which would be consistent with increased iceberg melting here. Still, we conclude that melting of excess sea ice is the main reason for the low salinity in the EWG.

[44] This contributes to the persistence of high productivity at this specific location by creating stratified conditions. However, primary production also requires the micronutrient iron, which has repeatedly been found to be limiting in Southern Ocean environments. Therefore, we investigate potential iron sources in the following section.

4.3. Potential Iron Sources

[45] In particulate plankton samples in the bloom area, we measured Fe/C ratios of $2*10^{-4}$ mol mol^{-1} (Table 1). The observed values for Fe/C ratios are exceptionally high for an open ocean system, which are usually expected to be in the order of 10^{-5} mol mol^{-1} or less [*Sunda and Huntsman*, 1995; *Twining et al.*, 2004]. We rule out sampling artifacts, because the type of 18,000 × g centrifuge used for the collection of particulate samples has previously been shown to be efficient and reliable in collecting trace element samples of marine particulate matter [*Schussler and Kremling*, 1993]. Inspection of the collected material by Scanning Electron Microscopy (SEM) with energy dispersive analysis of secondary X-rays (EDX) gave no evidence of contaminating terrigenous particles. Approximately 1/20 of the iron was found within the diatom shells, after cleaning from all potential traces of terrigenous matter. As the Fe/C ratio observed here exceeds known values of cellular iron requirements, we consider the possibility that a part of the iron may be present in adsorbed form, or there is a case of "luxury iron uptake and storage" [*Sunda and Huntsman*, 1995].

[46] With an organic carbon production of 2000 mmol*m^{-2} in the productive layer of the bloom, as derived from nutrient depletion, this corresponds to a particulate iron stock of 400 μmol m^{-2} (Table 1). Irrespective of the form of iron present in the particulate samples, we conclude that our inferred iron stock of 400 μmol m^{-2} must be supported by an efficient supply mechanism, as rapid water mass exchange and particle export limit residence times in this dynamic region. Particulate iron export might be less than the 25% (= 100 μmol m^{-2}) suggested by ^{234}Th export data (Table 1), if the Fe/C ratio in exported particles is lower than in suspended matter.

[47] Various pathways of iron to the Southern Ocean have been investigated recently, including airborne iron supply from terrestrial sources by dust [*Martínez-Garcia et al.*, 2009], supply from underlying water masses by deep upwelling and vertical mixing [*Meskhidze et al.*, 2007], detrital material and mixing effects from islands [*Blain et al.*, 2007], sea ice [*Lannuzel et al.*, 2008], melting icebergs [*Hegner et al.*, 2007; *Raiswell et al.*, 2008; *Smith et al.*, 2007] or extraterrestrial dust [*Johnson*, 2001].

[48] In order to assess the potential contribution from atmospheric deposition, we use published values of dust or iron in snow. *Lannuzel et al.* [2008] report concentrations of total dissolvable iron in snow on sea ice of up to 20 nM (= 1.1 ng/g) in the western Weddell Gyre, and similar and lower concentrations are found in Eastern Antarctic sea-ice environments [*Lannuzel et al.*, 2007]. *Schodlok et al.* [2005] calculate with a concentration of 10 ng/g dust in snow, which translates into 0.3 ng/g total iron assuming 3% iron in dust, a fraction of which will be dissolvable. No atmospheric iron deposition data are available from the immediate neighborhood of our study, but aerosol measurements at Neumayer station (70°39′S, 8°15′W) display strong dust flux maxima in austral summer [*Weller et al.*, 2008]. Summarizing, we assume an iron concentration of 0.5 ng/g in snow, and a deposition of 100 kg snow per m^2 of sea ice, after *Worby et al.* [2008]. This results in a contribution of 50 μg m^{-2} yr^{-1}, or ~1 μmol m^{-2} yr^{-1} onto sea ice, 0.25% of the iron stocks we find in the productive layer. Higher iron fluxes may be expected in the ice-free season, but these can only play a minor role for the ice melt related bloom observed here, and these fluxes could still only account for a small fraction of the iron stocks.

[49] Deep upwelling is also a source that might be of importance here, as it is prevalent in the WG, especially in its eastern and southern parts, and in the Maud Rise region. Therefore, we will investigate its potential impact based on our data. Typical deep water dissolved iron concentrations in the WG are in the order of 0.2–0.4 μmol/m^3 [*Boye et al.*, 2001; *Croot et al.*, 2004] at 18°E and 6°E, respectively. Vertical transports are high, with annual entrainment rates of deep water on the order of 50 m yr^{-1} [*Geibert et al.*, 2002; *Gordon and Huber*, 1990]. Calculating with the higher value (0.4 μmol/m^3), this means an approximate annual supply from below of ~20 μmol m^{-2} yr^{-1}, which corresponds to only 5% of the inferred stock in the bloom.

[50] We measured $^{227}Ac_{xs}$ (Table 1) to investigate whether the origin of the bloom-forming water mass in the EWG is indeed upwelled WG water, or rather water from the ACC. The uniquely high $^{227}Ac_{xs}$ values known from the WG allow discrimination of WG from ACC waters [*Geibert et al.*, 2002] despite the alteration in temperature and salinity characteristics by melting ice. Three out of seven $^{227}Ac_{xs}$ values at the WG/ACC boundary point to an ACC source (~0.25 dpm*m^{-3}), whereas the four other values indicate WG waters or mixtures. The highest $^{227}Ac_{xs}$ was in the northernmost part of the WG. Because high productivity spans both ACC and WG surface waters, we can state that deep upwelling in the WG does not seem to be the major iron source that controls this bloom, at least not without sea ice acting as a transporting agent. We can also infer from the $^{227}Ac_{xs}$ pattern that ACC waters can be found floating on underlying WG waters here.

[51] In order to evaluate the potential importance of sea ice for iron inputs, we take values of sea-ice iron concentrations typical for the western WG from the literature. In early spring, a depth-integrated total iron concentration of 59.4 μmol/m^{-2} was reported for sea ice [*Lannuzel et al.*, 2008]. Observations of iron release associated with the spring melt of sea ice from the WG at 6°E [*Croot et al.*, 2004] confirm that sea ice is indeed a likely transporting agent for iron in the WG. We concluded in the freshwater budget of our study (section 3.1) that the volume of sea ice delivered to the eastern boundary of the WG is at least 2.7 times higher than the regional average, associated with a higher than average iron supply of >160.4 μmol m^{-2}. Cumulative advection of sea ice to the EWG boundary, followed by melting when encountering warmer ACC waters, therefore accounts directly for 40% of the calculated particulate iron inventory of 400 μmol m^{-2}. Considering that the

sea-ice enrichment factor of 2.7 can be an underestimate because the freshwater lens spreads horizontally, and adding the uncertainty of highly variable iron concentrations in sea ice, and then taking into consideration internal recycling, the proposed mechanism can sustain the stock of 400 μmol m^{-2} Fe observed here, and create Fe levels that may be temporarily sufficient to alleviate iron limitation.

[52] Elevated iron levels in sea ice may be explained by sorption or uptake of dissolved iron, as depicted by *Lannuzel et al.* [2008]. However, sea ice can theoretically not contain more iron than delivered by upwelling and atmospheric fluxes together in winter. Therefore, we suggest a mechanism that delivers additional iron into sea ice during winter, when large icebergs continue melting due to their penetration into deeper water layers (up to >300 m). This means that they are exposed to warmer waters even during winter, when sea ce is present and growing. Continuous melting of icebergs in winter will lead to rising fresher and potentially iron-enriched waters from below, in the immediate vicinity of icebergs. This water would spread under the sea ice as a thin lens of fresher water, where it can refreeze due to its comparatively low salinity, and it can undergo processes of sorption and biological uptake. This hypothesis is consistent with maxima of iron concentrations in the lowermost parts of sea ice prior to the onset of spring melting [*Lannuzel et al.*, 2008], and the generally high iron concentration observed in sea ice that is not fully supported by atmospheric deposition and upwelling.

5. Conclusions

[53] Our data highlight the role of melting ice in the enhanced productivity in the EWG. We propose that production is supported by the persistent supply of sea ice and icebergs to the EWG boundary by wind-driven advection. Here, the encounter with warmer ACC waters results in rapid melting. This melting hot spot causes an enhanced input of iron and salinity-driven stratification of the surface waters. The resulting phytoplankton bloom is extensive and it constitutes a recurrent spring/summer feature that has not been well recognized before in either remote-sensing based estimates or coupled biophysical models.

[54] Productivity estimates derived using monthly composited data have been found here to underestimate in situ observations in the bloom region substantially at many stations. Monthly composited remote-sensing data should be used with caution at these latitudes, as intense seasonal blooms such as that described here are likely to be heavily undersampled owing to cloud and ice cover. The exclusion of partly sea ice containing pixels during data processing could cause a systematic undersampling of early spring blooms that are related to sea-ice cover, and if sea-ice-related blooms released a significant amount of dimethylsulfide, cloud cover could also be coupled to productivity [*Charlson et al.*, 1987], causing a bias in satellite observations. The high degree of cloudiness in this region alone means that monthly composites of satellite data represent the best means to study spatial patterns in the data, yet the patchiness caused by cloud cover together with the compositing over 4 weeks (longer than the residency of peak chlorophyll values during a bloom) together must result in a systematic underestimate of chlorophyll values in monthly satellite products. If such effects were responsible for the mismatch between satellite-based estimates and in situ data, they would also concern other areas with sea-ice-stimulated productivity.

[55] A persistent transport mechanism as described here can explain why modeling according to nutrient distributions yields a region of anomalously high export production at the EWG/ACC boundary. It is also consistent with anomalously high opal fluxes to marine sediments in the Indian Sector of the SO [*Geibert et al.*, 2005], which cannot be linked to upstream islands. The high productivity in the area would also be consistent with elevated whale abundances, as indicated by the historical whaling records. Our results imply that the expected shifts in sea-ice patterns due to global warming are likely to affect the regional distribution of biological productivity. The supply of limiting micronutrients by wind-driven sea ice and icebergs may have been active in other high-latitude HNLC areas, e.g., the northwest Pacific in the past, and may be active at present at other SO gyre systems.

[56] **Acknowledgments.** MODIS and SeaWiFS ocean color and sea surface temperature data were kindly provided by the MODIS Science Team, the Ocean Productivity Group, and by the NASA Ocean Color Team. SeaWiFS data were received in real time under scientific license courtesy of NASA and GeoEye. Isabelle Ansorge (team coordinator for UCT group), Sandy Thomalla, Rhys Gilliam, Nazeera Hargeyn, and the team of Gerhard Kattner contributed substantially to the nutrient and oxygen data set. Rita Froehlking assisted with the analysis of particulate samples. W.G. was supported by DFG projects RU712-4 and GE1118/2-2; he is currently supported by the Scottish Alliance for Geosciences, Environment and Society (SAGES). D.C.E.B. and M.H. were partly supported by the EU IP CARBOOCEAN (511176 (GOCE)). P.A. was supported by the Bremen International Graduate School for Marine Sciences (GLOMAR) funded by DFG (Excellence Initiative). We thank Ben Raymond, Corinne Le Quéré (AE), and an anonymous reviewer for their useful remarks. This work would have been impossible without the continuous support of Dieter K. Fütterer, chief scientist of the expedition, and the helpful crew of R/V *Polarstern*. In remembrance of Wolfgang Dinter.

References

Anderson, R. F., S. Ali, L. I. Bradtmiller, S. H. H. Nielsen, M. Q. Fleisher, B. E. Anderson, and L. H. Burckle (2009), Wind-driven upwelling in the Southern Ocean and the deglacial rise in atmospheric CO_2, *Science*, *323* (5920), 1443–1448, doi:10.1126/science.1167441.

Arrigo, K. R., G. L. van Dijken, D. G. Ainley, M. A. Fahnestock, and T. Markus (2002), Ecological impact of a large Antarctic iceberg, *Geophys. Res. Lett.*, *29*(7), 1104, doi:10.1029/2001GL014160.

Assmy, P., J. Henjes, C. Klaas, and V. Smetacek (2007), Mechanisms determining species dominance in a phytoplankton bloom induced by the iron fertilization experiment EisenEx in the Southern Ocean, *Deep Sea Res., Part I*, *54*(3), 340–362, doi:10.1016/j.dsr.2006.12.005.

Assmy, P., D. U. Hernandez-Becerril, and M. Montresor (2008), Morphological variability and life cycle traits of the type species of the diatom genus Chaetoceros, C-dichaeta, *J. Phycol.*, *44*(1), 152–163, doi:10.1111/j.1529-8817.2007.00430.x.

Bakker, D. C. E., M. C. Nielsdottir, P. J. Morris, J. Venables, and A. J. Watson (2007), The island mass effect and biological carbon uptake for the subantarctic Crozet Archipelago, *Deep Sea Res., Part II*, *54*(18–20), 2174–2190, doi:10.1016/j.dsr2.2007.06.009.

Bakker, D. C. E., M. Hoppema, M. Schröder, W. Geibert, and H. J. W. De Baar (2008), A rapid transition from ice covered CO_2-rich waters to a biologically mediated CO_2 sink in the eastern Weddell Gyre, *Biogeosciences*, *5*, 1373–1386, doi:10.5194/bg-5-1373-2008.

Bathmann, U. V., R. Scharek, C. Klaas, C. D. Dubischar, and V. Smetacek (1997), Spring development of phytoplankton biomass and composition in major water masses of the Atlantic sector of the Southern Ocean, *Deep Sea Res., Part II*, *44*(1–2), 51–67, doi:10.1016/S0967-0645(96)00063-X.

Behrenfeld, M. J., and P. G. Falkowski (1997), Photosynthetic rates derived from satellite-based chlorophyll concentration, *Limnol. Oceanogr.*, *42*(1), 1–20, doi:10.4319/lo.1997.42.1.0001.

Berger, W. H. (1989), Appendix: Global maps of ocean productivity, in *Productivity of the Ocean: Present and Past*, edited by W. H. Berger, V. S. Smetacek, and G. Wefer, pp. 429–455, John Wiley, New York.

Blain, S., et al. (2007), Effect of natural iron fertilization on carbon sequestration in the Southern Ocean, *Nature*, *446*(7139), 1070–1074, doi:10.1038/nature05700.

Boyd, P. W., et al. (2007), Mesoscale iron enrichment experiments 1993–2005: Synthesis and future directions, *Science*, *315*(5812), 612–617, doi:10.1126/science.1131669.

Boye, M., C. M. G. van den Berg, J. T. M. de Jong, H. Leach, P. Croot, and H. J. W. de Baar (2001), Organic complexation of iron in the Southern Ocean, *Deep Sea Res., Part I*, *48*(6), 1477–1497, doi:10.1016/S0967-0637(00)00099-6.

Charlson, R. J., J. E. Lovelock, M. O. Andreae, and S. G. Warren (1987), Oceanic phytoplankton, atmospheric sulfur, cloud albedo and climate, *Nature*, *326*(6114), 655–661, doi:10.1038/326655a0.

Cochran, J. K., and P. Masqué (2003), Short-lived U/Th series radionuclides in the ocean: Tracers for scavenging rates, export fluxes and particle dynamics, in uranium, *Rev. Mineral. Geochem.*, *52*, 461–492.

Croot, P. L., K. Andersson, M. Ozturk, and D. R. Turner (2004), The distribution and speciation of iron along 6 degrees E in the Southern Ocean, *Deep Sea Res., Part II*, *51*(22–24), 2857–2879, doi:10.1016/j.dsr2.2003.10.012.

Culberson, C. H. (1994), Dissolved oxygen. WOCE operations manual. WHP operations and methods: July 1991, *WHP Off. Rep. WHPO 91-1*, 15 pp., Woods Hole, Mass.

de Steur, L., D. M. Holland, R. D. Muench, and M. G. McPhee (2007), The warm-water "Halo" around Maud Rise: Properties, dynamics and Impact, *Deep Sea Res., Part I*, *54*(6), 871–896, doi:10.1016/j.dsr.2007.03.009.

Eicken, H. (1992), Salinity profiles of Antarctic sea ice: Field data and model results, *J. Geophys. Res.*, *97*(C10), 15,545–15,557, doi:10.1029/92JC01588.

Francois, R., M. A. Altabett, E. F. Yu, D. M. Sigman, M. P. Bacon, M. Frank, G. Bohrmann, G. Bareille, and L. D. Labeyrie (1997), Contribution of Southern Ocean surface-water stratification to low atmospheric CO_2 concentrations during the last glacial period, *Nature*, *389*(6654), 929–935, doi:10.1038/40073.

Garibotti, I. A., M. Vernet, W. A. Kozlowski, and M. E. Ferrario (2003), Composition and biomass of phytoplankton assemblages in coastal Antarctic waters: A comparison of chemotaxonomic and microscopic analyses, *Mar. Ecol. Prog. Ser.*, *247*, 27–42, doi:10.3354/meps247027.

Geibert, W., and I. Vöge (2008), Progress in the determination of ^{227}Ac in sea water, *Mar. Chem.*, *109*(3–4), 238–249, doi:10.1016/j.marchem.2007.07.012.

Geibert, W., M. M. Rutgers van der Loeff, C. Hanfland, and H. J. Dauelsberg (2002), Actinium-227 as a deep-sea tracer: Sources, distribution and applications, *Earth Planet. Sci. Lett.*, *198*(1–2), 147–165, doi:10.1016/S0012-821X(02)00512-5.

Geibert, W., M. M. Rutgers van der Loeff, R. Usbeck, R. Gersonde, G. Kuhn, and J. Seeberg-Elverfeldt (2005), Quantifying the opal belt in the Atlantic and southeast Pacific sector of the Southern Ocean by means of ^{230}Th normalization, *Global Biogeochem. Cycles*, *19*, GB4001, doi:10.1029/2005GB002465.

Geibert, W., M. Charette, G. Kim, W. S. Moore, J. Street, M. Young, and A. Paytan (2008), The release of dissolved actinium to the ocean: A global comparison of different end-members, *Mar. Chem.*, *109*(3–4), 409–420, doi:10.1016/j.marchem.2007.07.005.

Gladstone, R. M., G. R. Bigg, and K. W. Nicholls (2001), Iceberg trajectory modeling and meltwater injection in the Southern Ocean, *J. Geophys. Res.*, *106*(C9), 19,903–19,915, doi:10.1029/2000JC000347.

Gordon, A. L., and B. A. Huber (1990), Southern Ocean winter mixed layer, *J. Geophys. Res.*, *95*(C7), 11,655–11,672, doi:10.1029/JC095iC07p11655.

Gouretski, V. V., and A. I. Danilov (1993), Weddell Gyre: Structure of the eastern boundary, *Deep Sea Res., Part I*, *40*(3), 561–582, doi:10.1016/0967-0637(93)90146-T.

Grasshoff, K. K. K., and M. Ehrhardt (1983), *Methods of Seawater Analysis*, 2nd ed., Verlag Chemie, Weinheim, Deerfield Beach, Fla.

Hegner, E., H. J. Dauelsberg, M. M. R. van der Loeff, C. Jeandel, and H. J. W. de Baar (2007), Nd isotopic constraints on the origin of suspended particles in the Atlantic sector of the Southern Ocean, *Geochem. Geophys. Geosyst.*, *8*, Q10008, doi:10.1029/2007GC001666.

Helmke, P., O. Romero, and G. Fischer (2005), Northwest African upwelling and its effect on offshore organic carbon export to the deep sea, *Global Biogeochem. Cycles*, *19*, GB4015, doi:10.1029/2004GB002265.

Hoppema, M. (2004), Weddell Sea is a globally significant contributor to deep-sea sequestration of natural carbon dioxide, *Deep Sea Res., Part I*, *51*(9), 1169–1177, doi:10.1016/j.dsr.2004.02.011.

Hoppema, M., and L. Goeyens (1999), Redfield behavior of carbon, nitrogen, and phosphorus depletions in Antarctic surface water, *Limnol. Oceanogr.*, *44*(1), 220–224, doi:10.4319/lo.1999.44.1.0220.

Hoppema, M., H. J. W. de Baar, R. G. J. Bellerby, E. Fahrbach, and K. Bakker (2002), Annual export production in the interior Weddell Gyre estimated from a chemical mass balance of nutrients, *Deep Sea Res., Part II*, *49*(9–10), 1675–1689, doi:10.1016/S0967-0645(02)00006-1.

Hutchins, D. A., and K. W. Bruland (1998), Iron-limited diatom growth and Si: N uptake ratios in a coastal upwelling regime, *Nature*, *393*(6685), 561–564, doi:10.1038/31203.

Johnson, K. S. (2001), Iron supply and demand in the upper ocean: Is extraterrestrial dust a significant source of bioavailable iron?, *Global Biogeochem. Cycles*, *15*(1), 61–63, doi:10.1029/2000GB001295.

Jongma, J. I., E. Driesschaert, T. Fichefet, H. Goosse, and H. Renssen (2009), The effect of dynamic-thermodynamic icebergs on the Southern Ocean climate in a three-dimensional model, *Ocean Modell.*, *26*(1–2), 104–113.

Kang, S. H., and G. A. Fryxell (1993), Phytoplankton in the Weddell Sea, Antarctica: Composition, abundance and distribution in water-column assemblages of the marginal ice-edge zone during austral autumn, *Mar. Biol. Berlin*, *116*(2), 335–348, doi:10.1007/BF00350024.

Kattner, G. (1999), Storage of dissolved inorganic nutrients in seawater: Poisoning with mercuric chloride, *Mar. Chem.*, *67*(1–2), 61–66, doi:10.1016/S0304-4203(99)00049-3.

Kimura, N. (2004), Sea ice motion in response to surface wind and ocean current in the Southern Ocean, *J. Meteorol. Soc. Jpn.*, *82*(4), 1223–1231, doi:10.2151/jmsj.2004.1223.

Kirk, J. T. O. (1994), *Light and Photosynthesis in Aquatic Ecosystems*, Cambridge Univ. Press, Cambridge, U. K., doi:10.1017/CBO9780511623370.

Lannuzel, D., V. Schoemann, J. de Jong, J. L. Tison, and L. Chou (2007), Distribution and biogeochemical behaviour of iron in the East Antarctic sea ice, *Mar. Chem.*, *106*(1–2), 18–32, doi:10.1016/j.marchem.2006.06.010.

Lannuzel, D., V. Schoemann, J. de Jong, L. Chou, B. Delille, S. Becquevort, and J. L. Tison (2008), Iron study during a time series in the western Weddell pack ice, *Mar. Chem.*, *108*(1–2), 85–95, doi:10.1016/j.marchem.2007.10.006.

Leynaert, A., D. M. Nelson, B. Queguiner, and P. Treguer (1993), The silica cycle in the Antarctic Ocean: Is the Weddell Sea atypical?, *Mar. Ecol. Prog. Ser.*, *96*(1), 1–15, doi:10.3354/meps096001.

Lichey, C., and H. H. Hellmer (2001), Modeling giant-iceberg drift under the influence of sea ice in the Weddell Sea, Antarctica, *J. Glaciol.*, *47*(158), 452–460, doi:10.3189/172756501781832133.

Marinov, I., A. Gnanadesikan, J. R. Toggweiler, and J. L. Sarmiento (2006), The Southern Ocean biogeochemical divide, *Nature*, *441*(7096), 964–967, doi:10.1038/nature04883.

Martínez-Garcia, A., A. Rosell-Melé, W. Geibert, V. Gaspari, P. Masqué, R. Gersonde, and C. Barbante (2009), Links between iron supply, ocean productivity, sea surface temperature, and CO_2 over the last 1.1 Ma, *Paleoceanography*, *24*, PA1207, doi:10.1029/2008PA001657.

Martinson, D. G., and R. A. Iannuzzi (2003), Spatial/temporal patterns in Weddell gyre characteristics and their relationship to global climate, *J. Geophys. Res.*, *108*(C4), 8083, doi:10.1029/2000JC000538.

Meskhidze, N., A. Nenes, W. L. Chameides, C. Luo, and N. Mahowald (2007), Atlantic Southern Ocean productivity: Fertilization from above or below?, *Global Biogeochem. Cycles*, *21*, GB2006, doi:10.1029/2006GB002711.

Morel, A., and J. F. Berthon (1989), Surface pigments, algal biomass profiles, and potential production of the euphotic layer: Relationships reinvestigated in view of remote-sensing applications, *Limnol. Oceanogr.*, *34*(8), 1545–1562, doi:10.4319/lo.1989.34.8.1545.

Mueller, P. J., and R. Schneider (1993), An automated leaching method for the determination of opal in sediments and particulate matter, *Deep Sea Res., Part I*, *40*(3), 425–444, doi:10.1016/0967-0637(93)90140-X.

Nozaki, Y. (1984), Excess ^{227}Ac in deep ocean water, *Nature*, *310*, 486–488, doi:10.1038/310486a0.

Nozaki, Y. (1993), Actinium-227: A steady state tracer for the deep-sea basin-wide circulation and mixing studies, in *Deep Ocean Circulation:*

Physical and Chemical Aspects, edited by T. Teramoto, pp. 139–155, Elsevier, New York, doi:10.1016/S0422-9894(08)71323-0.

Orsi, A. H., T. Whitworth, and W. D. Nowlin (1995), On the meridional extent and fronts of the Antarctic Circumpolar Current, *Deep Sea Res., Part I*, *42*(5), 641–673, doi:10.1016/0967-0637(95)00021-W.

Pichevin, L., B. C. Reynolds, R. Ganeshram, I. Cacho, L. Pena, K. Keefe, and R. M. Ellam (2009), Enhanced carbon pump inferred from relaxation of nutrient limitation in the glacial ocean, *Nature*, *459*, 1114–1117, doi:10.1038/nature08101.

Ragueneau, O., S. Schultes, K. Bidle, P. Claquin, and B. La Moriceau (2006), Si and C interactions in the world ocean: Importance of ecological processes and implications for the role of diatoms in the biological pump, *Global Biogeochem. Cycles*, *20*, GB4S02, doi:10.1029/2006GB002688.

Raiswell, R., L. G. Benning, M. Tranter, and S. Tulaczyk (2008), Bioavailable iron in the Southern Ocean: The significance of the iceberg conveyor belt, *Geochem. Trans.*, *9*(7), 9 pp., doi:10.1186/1467-4866-9-7.

Rutgers van der Loeff, M. M., and W. S. Moore (1999), Determination of natural radioactive tracers, in *Methods of Seawater Analysis*, edited by K. K. Grasshoff and M. M. Ehrhardt, pp. 365–397, Wiley, Weinheim, New York.

Savidge, G., J. Priddle, L. C. Gilpin, U. Bathmann, E. J. Murphy, N. J. P. Owens, R. T. Pollard, D. R. Turner, C. Veth, and P. Boyd (1996), An assessment of the role of the marginal ice zone in the carbon cycle of the Southern Ocean, *Antarct. Sci.*, *8*(4), 349–358, doi:10.1017/S0954102096000521.

Savoye, N., C. Benitez-Nelson, A. B. Burd, J. K. Cochran, M. Charette, K. O. Buesseler, G. A. Jackson, M. Roy-Barman, S. Schmidt, and M. Elskens (2006), Th-234 sorption and export models in the water column: A review, *Mar. Chem.*, *100*(3–4), 234–249, doi:10.1016/j.marchem.2005.10.014.

Schlitzer, R. (2002), Carbon export fluxes in the Southern Ocean: Results from inverse modeling and comparison with satellite-based estimates, *Deep Sea Res., Part II*, *49*(9–10), 1623–1644, doi:10.1016/S0967-0645(02)00004-8.

Schodlok, M. P., H. H. Hellmer J. Schwarz, and T. Busche (2005), On iceberg behaviour: Observations, model results, and satellite data, *FRISP Rep. 16*, Forum for Res. into Ice Shelf Proc., Bjerknes Cent. for Clim. Res. and Geophys. Inst., Bergen, Norway.

Schodlok, M. P., H. H. Hellmer, G. Rohardt, and E. Fahrbach (2006), Weddell Sea iceberg drift: Five years of observations, *J. Geophys. Res.*, *111*, C06018, doi:10.1029/2004JC002661.

Schröder, M., and E. Fahrbach (1999), On the structure and the transport of the eastern Weddell Gyre, *Deep Sea Res., Part II*, *46*(1–2), 501–527, doi:10.1016/S0967-0645(98)00112-X.

Schussler, U., and K. Kremling (1993), A pumping system for underway sampling of dissolved and particulate trace elements in near-surface waters, *Deep Sea Res., Part I*, *40*(2), 257–266, doi:10.1016/0967-0637(93)90003-L.

Schwarz, J. N., and M. P. Schodlok (2009), Impact of drifting icebergs on surface phytoplankton biomass in the Southern Ocean: Ocean colour remote sensing and in situ iceberg tracking, *Deep Sea Res., Part I*, *56*(10), 1727–1741, doi:10.1016/j.dsr.2009.05.003.

Sigman, D. M., and E. A. Boyle (2000), Glacial/interglacial variations in atmospheric carbon dioxide, *Nature*, *407*(6806), 859–869, doi:10.1038/35038000.

Smetacek, V., C. Klaas, S. Menden-Deuer, and T. A. Rynearson (2002), Mesoscale distribution of dominant diatom species relative to the hydrographical field along the Antarctic Polar Front, *Deep Sea Res., Part II*, *49*(18), 3835–3848, doi:10.1016/S0967-0645(02)00113-3.

Smith, K. L., B. H. Robison, J. J. Helly, R. S. Kaufmann, H. A. Ruhl, T. J. Shaw, B. S. Twining, and M. Vernet (2007), Free-drifting icebergs: Hot spots of chemical and biological enrichment in the Weddell Sea, *Science*, *317*(5837), 478–482, doi:10.1126/science.1142834.

Smith, W. O., and J. C. Comiso (2008), Influence of sea ice on primary production in the Southern Ocean: A satellite perspective, *J. Geophys. Res.*, *113*, C05S93, doi:10.1029/2007JC004251.

Smith, W. O., and D. M. Nelson (1985), Phytoplankton bloom produced by a receding ice edge in the Ross Sea: Spatial coherence with the density field, *Science*, *227*(4683), 163–166, doi:10.1126/science.227.4683.163.

Sokolov, S. (2008), Chlorophyll blooms in the Antarctic Zone south of Australia and New Zealand in reference to the Antarctic Circumpolar Current fronts and sea ice forcing, *J. Geophys. Res.*, *113*, C03022, doi:10.1029/2007JC004329.

Stephens, B. B., and R. F. Keeling (2000), The influence of Antarctic sea ice on glacial-interglacial CO_2 variations, *Nature*, *404*(6774), 171–174, doi:10.1038/35004556.

Sunda, W. G., and S. A. Huntsman (1995), Iron uptake and growth limitation in oceanic and coastal phytoplankton, *Mar. Chem.*, *50*(1–4), 189–206, doi:10.1016/0304-4203(95)00035-P.

Takeda, S. (1998), Influence of iron availability on nutrient consumption ratio of diatoms in oceanic waters, *Nature*, *393*(6687), 774–777, doi:10.1038/31674.

Tournadre, J., K. Whitmer, and F. Girard-Ardhuin (2008), Iceberg detection in open water by altimeter waveform analysis, *J. Geophys. Res.*, *113*, C08040, doi:10.1029/2007JC004587.

Tsuda, A., et al. (2003), A mesoscale iron enrichment in the western Subarctic Pacific induces a large centric diatom bloom, *Science*, *300*(5621), 958–961, doi:10.1126/science.1082000.

Twining, B. S., S. B. Baines, N. S. Fisher, and M. R. Landry (2004), Cellular iron contents of plankton during the Southern Ocean Iron Experiment (SOFeX), *Deep Sea Res., Part I*, *51*, 1827–1850, doi:10.1016/j.dsr.2004.08.007.

Tynan, C. T. (1998), Ecological importance of the southern boundary of the Antarctic Circumpolar Current, *Nature*, *392*(6677), 708–710, doi:10.1038/33675.

Uotila, J., T. Vihma, and J. Launiainen (2000), Response of the Weddell Sea pack ice to wind forcing, *J. Geophys. Res.*, *105*(C1), 1135–1151, doi:10.1029/1999JC900265.

Usbeck, R., M. R. van der Loeff, M. Hoppema, and R. Schlitzer (2002), Shallow remineralization in the Weddell Gyre, *Geochem. Geophys. Geosyst.*, *3*(1), 1008, doi:10.1029/2001GC000182.

Utermöhl, H. (1958), Zur Vervollkommnung der quantitativen Phytoplankton-Methodik, *Mitteil. Int. Ver. Limnol.*, *9*, 1–38.

Weller, R., J. Woltjen, C. Piel, R. Resenberg, D. Wagenbach, G. Konig-Langlo, and M. Kriews (2008), Seasonal variability of crustal and marine trace elements in the aerosol at Neumayer station, Antarctica, *Tellus, Ser. B*, *60*(5), 742–752, doi:10.1111/j.1600-0889.2008.00372.x.

Worby, A. P., C. A. Geiger, M. J. Paget, M. L. Van Woert, S. F. Ackley, and T. L. DeLiberty (2008), Thickness distribution of Antarctic sea ice, *J. Geophys. Res.*, *113*, C05S92, doi:10.1029/2007JC004254.

Wright, S. W., S. W. Jeffrey, R. F. C. Mantoura, C. A. Llewellyn, T. Bjornland, D. Repeta, and N. Welschmeyer (1991), Improved HPLC method for the analysis of chlorophylls and carotenoids from marine phytoplankton, *Mar. Ecol. Prog. Ser.*, *77*(2–3), 183–196, doi:10.3354/meps077183.

P. Assmy, C. Hanfland, M. Hoppema, M. Schröder, and I. Stimac, Alfred Wegener Institute for Polar and Marine Research, Postfach 120161, D-27515 Bremerhaven, Germany.

D. C. E. Bakker, School of Environmental Sciences, University of East Anglia, Norwich NR4 7TJ, UK.

W. Geibert and L. Pichevin, Grant Institute, School of Geosciences, University of Edinburgh, West Mains Road, Edinburgh EH9 3JW, UK. (walter.geibert@ed.ac.uk)

J. N. Schwarz, National Institute for Water and Atmosphere Research, Private Bag 14901, Wellington, New Zealand.

R. Usbeck, FIELAX GmbH, Barkhausenstr. 4, Bremerhaven D-27568, Germany.

A. Webb, Department of Oceanography, University of Cape Town, Private Bag X3, Cape Town 7701, South Africa.